Atmospheric Research 218 (2019) 70–77

Contents lists available at ScienceDirect

Atmospheric Research

journal homepage: www.elsevier.com/locate/atmosres

Impacts of distribution patterns of cloud optical depth on the calculation of radiative forcing

Yilun Chen, Kezhen Chong, Yunfei Fu*

School of Earth and Space Sciences, University of Science and Technology of China, Hefei 230026, China

ARTICLE INFO

Keywords:
Distribution pattern
Cloud optical depth
Radiative forcing
MODIS
Grid

ABSTRACT

The gridding process applied to satellite-retrieved cloud properties results in the loss of certain information. In this study, we analyzed the error associated with using gridded cloud optical depth (τ) in calculating radiative forcing from the perspective of the distribution pattern of τ. Utilizing the simulated results from SBDART (Santa Babara DISORT Atmospheric Radiative Transfer), we calculated this error in ideal probability distribution functions (PDFs) of τ while keeping the average τ constant, and then used the τ retrieved from MODIS (Moderate Resolution Imaging Spectroradiometer) pixel-level observations to simulate real case studies. The results from both the ideal experiments and real case studies indicate that there is a large dependence of the error caused by gridding process on the PDF of τ. The greatest relative error occurs in the cases when τ fits a two-point or uniform distribution, reaching 10–20%, while this error is below 5% when τ follows a binomial distribution. From the analysis of MODIS pixel-level data from June 2016, we found that the PDFs of τ within one grid point ($1^{\circ} \times 1^{\circ}$) could not be simply described by a normal distribution. Although using the logarithmic mean of τ controls the error effectively, the error can still be up to 4%. Our study suggests that using gridded data (especially the arithmetic mean) to calculate radiative forcing may result in uncertainty to a certain extent, which depends strongly on the distribution pattern of cloud properties within the grid point. The PDF of cloud properties should be comprehensively considered in the gridding process in the future.

1. Introduction

Clouds cover about two-thirds of Earth, and changes in their macro and micro characteristics affect radiative transfer in the atmosphere. Theoretically, cloud reflects inward shortwave solar radiation, thus cooling the Earth system, and reduces outward longwave radiation, thus heating the Earth system (Baker, 1997). For example, the Earth Radiation Budget Experiment (ERBE) observations show that in April 1985, the global average cloud shortwave radiative forcing ($-44.5\,\mathrm{W\,m^{-2}}$) was greater than its longwave radiative forcing ($31.3\,\mathrm{W\,m^{-2}}$), that is, during this period the net radiative forcing of cloud was negative (cooling effect) (Ramanthan, 1989). Different clouds have different cloud-top heights, morphologies, particle sizes, optical depths, and precipitation probabilities (Rangno and Hobbs, 2005), so their effects on radiation are also significantly different. The cloud optical depth (τ) is one of the cloud properties, reflecting the attenuation of radiation intensity by the medium in the transmission path, which directly affects the radiation budget of the ground-gas system (Curry and Ebert, 1992; Liou, 2002). The large coverage of cloud and its direct impact on radiation makes the study of cloud radiative forcing (RF) an important part of climate-related research.

Owing to the large horizontal and vertical distribution of clouds, the retrieval of cloud parameters from satellite observations has become an important foundation for related research. Combining the radiative transfer model and the reflectivity equation, Nakajima and King (1990) obtained a method for retrieving τ and the effective particle radius (R_e) using the reflection function of the visible and near-infrared bands, and further developed a three-channel algorithm (Nakajima and Nakajima, 1995). This algorithm is now applied to the retrieval of cloud properties on Moderate Resolution Imaging Spectroradiometer (MODIS) data (King et al., 1997), and has been widely used in the fields of cloud and precipitation features, cloud climatic effects, and aerosol indirect effects (Rossow and Schiffer, 1999; Rosenfeld et al., 2007; Fu, 2014).

Based on these algorithms and radiation transfer models, some researchers have studied the effects of clouds with different τ on the radiation budget. For example, Chen et al. (2000) simulated the annual mean radiative effects of nine types of clouds identified by the International Satellite Cloud Climatology Project (ISCCP), finding that stratocumulus, altostratus, and cirrostratus cloud with moderate optical thickness ($3.6 < \tau < 23$) have the largest impacts on shortwave RF. Li

* Corresponding author.
E-mail address: fyf@ustc.edu.cn (Y. Fu).

https://doi.org/10.1016/j.atmosres.2018.11.007
Received 21 July 2018; Received in revised form 7 November 2018; Accepted 11 November 2018
Available online 13 November 2018

et al. (2014) found that the cirrus boundary region ($\tau < 0.3$) also affects radiation, and its presence causes longwave RF of about 10 W m^{-2}. Fu et al. (2017) further found that the influence of this cirrus boundary on the global average longwave warming effect is approximately 0.07 W m^{-2}, which has not yet been considered in the Intergovernmental Panel on Climate Change assessment reports. Recently, some studies have used models to simulate the RF of cirrus clouds, cloud anvils, and precipitation clouds with different τ (Kienast-Sjogren et al., 2016; Yang et al., 2017; Chen and Fu, 2018), providing some new insights into the RF of clouds.

Owing to different orbits, scanning methods, and instrument performance, the horizontal resolutions of different spaceborne instruments are also different. For instance, the nadir point of the Visible and Infrared Scanner (VIRS) on Tropical Rainfall Measuring Mission (TRMM) has a horizontal resolution of 2 km; the resolution of the very high resolution scanning radiometer (AVHRR) is 1.09 km; MODIS on the Aqua/Terra satellite has three resolutions of 250 m (bands 1–2), 500 m (bands 3–7), and 1 km (bands 8–36) at nadir, and the size of the pixels can change significantly with higher scan angles. However, climate research tends to use large-scale grid data, such as the global radiative budget of the atmosphere of 10° × 10°, satellite-based global hydrological cycle observations of 1° × 1°, and global radiative balance based on weather analyses of 2.5° × 2.5°, which requires averaging the pixel-level data over the grid points (de la Torre Juarez et al., 2011). At the same time, the space–time average of pixel-level data within the grid points can also reduce the amount of data and alleviate the calculation workload.

Although there are many obvious advantages to data gridding, the resulting deviations from the original data cannot be ignored (Pierrehumbert, 1996). Oreopoulos et al. (2009) used MODIS 1°-gridded τ and R_e data, combined with radiative transfer models, to calculate the computational error of RF from the plane-parallel homogeneous approximation. They found the global average RF difference to be 6 W m^{-2} at the top of the atmosphere. de la Torre Juarez et al. (2011) used MODIS data to analyze cloud parameters with a horizontal scale from 5 km to 500 km and found that the global mean value of the cloud water path changes by 7%, which is likely to affect the calculation of global radiation budget. Chen and Fu (2017) revealed that even if the VIRS pixel (~2 km) is matched and arithmetically averaged to the precipitation radar pixel (~5 km), it will also cause a "partial filling effect", that is, a warm-rain pixel determined by the coarser resolution (~5 km) might actually contain clear-sky or cold-cloud pixel (~2 km).

The influence of cloud-parameter scale changes on RF has received widespread attention. Some studies have suggested the best scale for cloud-parameter studies based on theory or practical observations. For example, Oreopoulos and Davies (1998) suggested that the retrieving scales of optical thickness should be controlled within a few kilometers, which can reduce the "small-scale effect" (Cahalan et al., 1994). However, at present, there are still many relevant radiation studies that use gridded cloud parameters as the model input, which will undoubtedly bring systematic errors to the final result. In addition, numerous studies use the mean value to represent the cloud parameters within the grid, which is essentially based on the assumption of a normal distribution of cloud parameters (Roe and Baker, 2007), but this hypothesis may not have any theoretical basis (Hannart et al., 2009). For the same mean value in a grid, the probability distribution functions (PDFs) of cloud parameters may not be the same, and thus the influence on radiation will be different. In this study, the concept of gridded cloud-parameter distribution is introduced. First, the influence of different τ distributions on RF under ideal conditions is simulated. Then, using MODIS observations, the RF differences between before and after gridding are examined.

2. Data and methodology

The sixth-edition cloud product data (MOD06L2) derived from the Terra's MODIS measurements (accessible from https://modis.gsfc.nasa.gov/) are used in this study. These data are the basic item of the MODIS product, including the cloud-top parameters (pressure, temperature and height) and cloud properties (τ, R_e, etc.) (Platnick et al., 2017). MOD06_L2 is pixel-level data. Along the orbit, MODIS generates a photo every five minutes. The width of the scan track is about 2330 km, and the resolution of the cloud optical parameters is 1 km × 1 km. The Terra satellite, launched jointly by the United States, Japan, and Canada on 18 December 1999, is the first satellite of the Earth Observation System (EOS) program. The satellite is in the sun-synchronous polar orbit, with a period of 99 min (16 tracks per day), and transits the Equator at 10:30 and 22:30 (local time) every day. Because τ is dependent on the observation of the visible channel, cloud parameters can be retrieved only at 10:30 local time.

SBDART (Santa Babara DISORT Atmospheric Radiative Transfer) is a software for calculating plane-parallel atmospheric radiation transmission. It is built on FORTRAN programs, and is a collection of advanced and complex physical models including Discrete-Ordinate-Method Radiative Transfer (DISORT) (Stamnes et al., 1988). SBDART sets a reasonable default value for many variables. When the INPUT file is not set, the SBDART model will use the default value for calculation (Ricchiazzi et al., 1998).

Factors that affectthe cloud RF are not only τ, but also cloud height, R_e, surface albedo, and ambient temperature. However, these are not the focus of this study, so the variables need to be fixed to avoid mistaking their effects as that of τ on the RF. Unless otherwise specified, the variables are based on the default values provided by SBDART. To be as consistent as possible with the real cases, in the SBDART simulation, the atmospheric profile is selected as mid-latitude summer. In an ideal experiment, the effective particle radius is unified to 15 μm, and the solar zenith angles (SZA) are set to 0°, 30°, 60°, and 90°, respectively. Please note that "SAZ = 90°" is an artificial setting in model and represents the "night", in which case the shortwave solar radiation is turned off and only longwave radiation is considered. In the real cases, both the R_e and the SZA use the average value within the 1° grid provided by MOD06_L2.

Relative error, also called percent error, is used to put error into perspective. Here, let the absolute error be the difference between the inaccurate value and true value, and then the relative error is the absolute error divided by the true value. For example, an error of 1 W m^{-2} would be a lot if the true RF is 5 W m^{-2} (relative error is 20%), but insignificant if the RF is 1000 W m^{-2} (relative error is 20%).

3. Ideal experiment

We considered three typical patterns of distributions as possible PDFs of τ, which are two-point distribution, binomial distribution, and uniform distribution. We define x as τ, and $\bar{x}$ as the mean of τ, so that these three distributions are defined as follows.

(1) Two-point distribution

There are only two possible values for x, and the probability of each is 1/2. To be closer to the reality, we select the two points to be 0.5 times and 1.5 times the mean value, respectively, as shown in the formula below.

$$x \in \{0.5\bar{x},\ \ 1.5\bar{x} \mid \bar{x} = 2\text{n},\ \ \text{n} \in [1,\ \ 50] \cap \mathbb{Z}$$

The two-point distribution is the ideal form of bimodal distribution. For example, the cloud-top height usually obeys this distribution: there are two main peaks of 2 km and 14 km over the tropical ocean (Riley and Mapes, 2009) and a similar bimodal distribution is also found in the flat Gangetic Plains (Chen et al., 2017).

(2) Binomial distribution

For independent experiments repeated n times with the same conditions, the probability of occurrence of event A in each experiment is p.

X indicates the number of occurrences of event A in the n experiments, X may take 0, 1, 2, …, n, so that:

$$P(X = i) = C_n^i p^i (1-p)^{n-i}$$

The PDF of X is defined as the binomial distribution. Having considered the calculation step of SBDART and our experiment being comparable to the two-point distribution, we define n (that is, the maximum boundary of the PDF) to be twice as large as x, and $p = .5$ (i.e. the most ideal binomial distribution). The mathematical expression is as follows:

$$x \in [0, n] \cap x \in \mathbb{R} | \ n = 2\overline{x}$$

$$P(x = x_1) = C_n^{x_1} \times 0.5^n$$

When n is large enough, this distribution will approach a Poisson distribution, and when the step length approaches zero, the distribution changes from discrete to continuous, becoming a normal distribution, which is also the most common distribution pattern in atmospheric science. Similarly, this distribution hypothesis is also widely used in the assumptions of random variables in systems science (Liu et al., 2017).

(3) Uniform distribution

The uniform distribution is defined as the probability of all possible outcomes is the same. To simplify the simulation process, the step of τ is set to 1, and the distribution range is 0 to 2 times the mean τ. That is:

$$x \in [0, n] \cap x \in \mathbb{R} | \ n = 2\overline{x}$$

$$P(x = x_1) = \frac{1}{n+1}$$

The uniform distribution is one of the simplest distributions, the significance of which is that the probability of distribution of any interval of the same length is equal.

To clearly illustrate the three distributions described in this paper, we take $\overline{x}$ (mean τ) as an example. Fig. 1 shows the PDFs of the three distributions, with the mean τ as 10.

According to the conditions described in the Section 2, we simulated the surface RF corresponding to different τ when the SZA is 0°, 30°, 60°, and 90°. The RF corresponding to different distribution patterns at this time can also be obtained when the arithmetic mean of τ is fixed at a constant value. For example, when the average τ is 10, the RF of the two-point distribution is the average of the RF with a τ of 5 and another of 15; and the RF corresponding to the binomial distribution is the weighted average of the RFs of τ from 0 to 20 (weight coefficients are the probability in Fig. 1b, and $\tau = 0$ means clear sky).

Assume a grid cell contains many pixels, and the cloud optical depth of each pixel is τ_1, τ_2, … τ_N, respectively (Fig. 2). Then, we have two methods to calculate the RF within a grid cell. One is using each pixel-level τ to calculate the pixel-level RF, and then averaging these RFs to get RF_a (left), which should represent the accurate RF, but the calculation is complicated. Another is averaging the τ in a grid cell to get $\overline{\tau}$ first, and then calculate the RF_b by using $\overline{\tau}$ directly (right). This method is widely used in most studies, but it produces errors because of the inhomogeneous distribution of τ.

Fig. 3 shows the RF under the different distributions of τ (green line for two-point distribution, blue line for binomial distribution, and red line for binomial distribution), and calculated by directly using grid-mean τ without considering the distribution pattern or weights (black line). Please note that the RFs of green, blue and red lines are calculated by using the left method in Fig. 2 (RF_a), and the black line is from the right method in Fig. 2 (RF_b). Therefore, the three typical distribution patterns are presupposed as the accurate values, to evaluate under which condition would the RF calculated by gridded τ produce the greatest error.

During the day, the surface RF of cloud is negative, that is, it has a cooling effect. This is mainly because the cloud blocks the sunlight, so that the shortwave radiation that passes through the cloud to the surface is less than the condition without cloud. As τ increases, more and more sunlight is reflected by the cloud, and the negative RF of the cloud increases gradually. When τ is small, the change rate of the RF is large, and when τ is > 30, the change rate is significantly decreased, and the RF gradually stabilizes. As the SZA increases, the injected shortwave radiation decreases, and the RF value also decreases. At a SZA of 0°, the surface RF is stable at 900–1000 W m^{-2} (Fig. 3a), while at a SZA of 60°, it is reduced by half and stabilized at ~400 W m^{-2} (Fig. 3c). At night (i.e. SZA = 90°), there is no shortwave radiation input, so the longwave radiation from the surface dominates, thus making the cloud mainly have a greenhouse effect. As τ increases, the cloud's blocking effect on longwave radiation is strengthened and RF increases rapidly, which stabilizes when τ is > 10. It can also be seen from the Fig. 3 that the variation of the RF with τ is nonlinear regardless of day or night. Simply calculating the arithmetic average of the τ in the grid point will inevitably cause a deviation in the calculation of RF.

The RF values are not comparable for different conditions, so we calculated the relative errors instead. The error of the binomial distribution is the smallest, mainly below 5%; the error of the uniform distribution is the greatest, which is up to 14% during the day and 20% at night; the error of the two-point distribution is slightly smaller than the uniform distribution, up to 10%. It indicates that using RF calculated from grid-mean τ produces the greatest error when the τ in grid obeys uniform distribution. This phenomenon can be attributed to the feature of the lines in Fig. 3a, that is, RF(τ) is a "convex downward" function in a Euclidean space. More generally, the slope of the lines is not constant but monotonically non-decreasing (its absolute value monotonically decreasing) for τ from 2 to 100, which leads to the fact that the distribution with more small τ values will cause greater error. At the same time, the error function corresponding to the three distribution patterns has the same trend as τ, and the maximum error is reached at the smallest τ value. For example, when SZA is 0°, τ is 7–8 in the binomial distribution when the relative error becomes largest; for

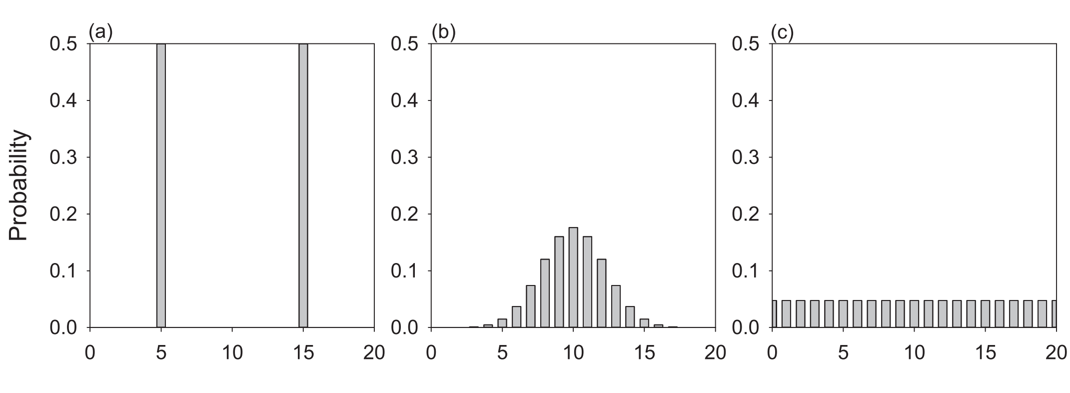

Fig. 1. For an average τ of 10, the probability of τ in: (a) two-point distribution, (b) binomial distribution, and (c) uniform distribution.

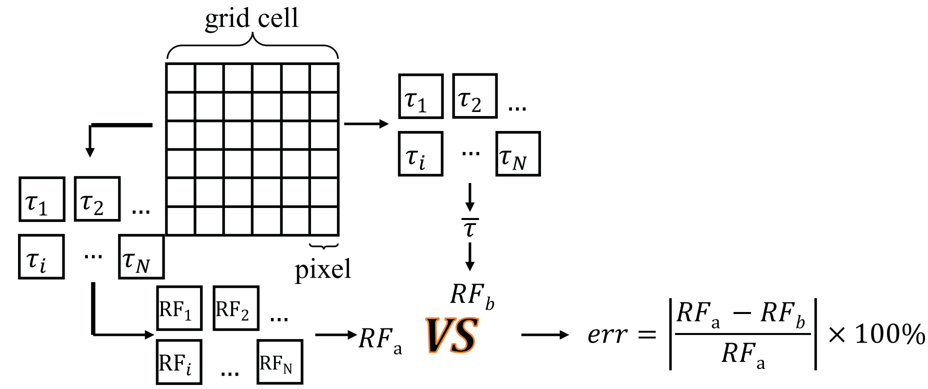

Fig. 2. Flowchart of the relative error calculation.

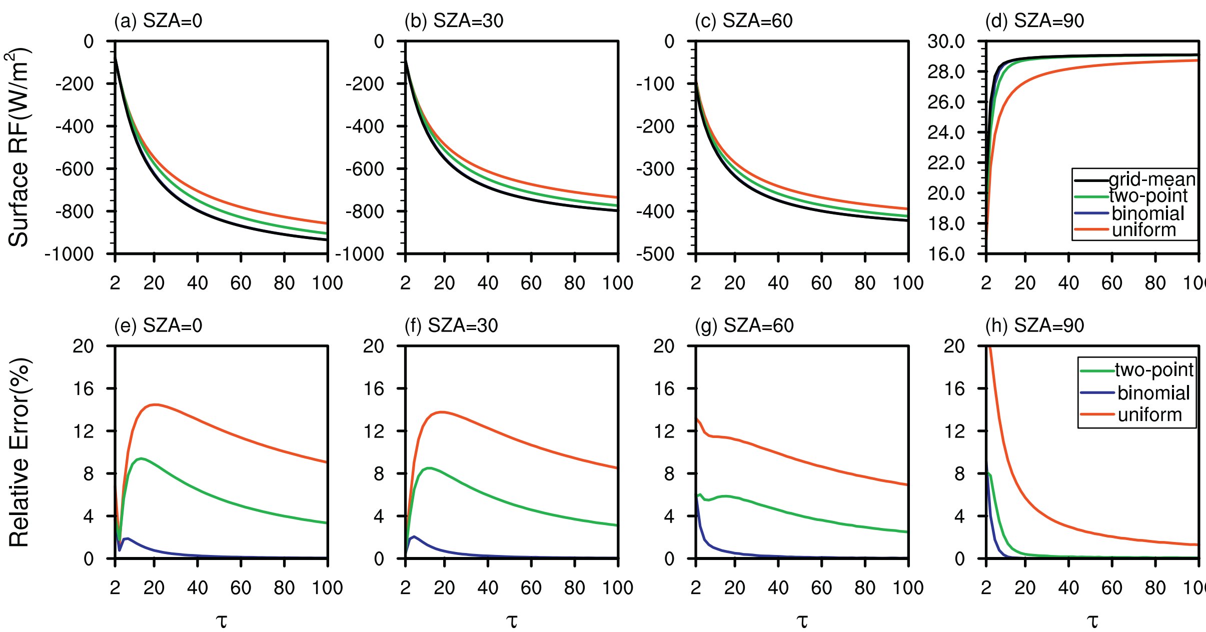

Fig. 3. Surface RF (a–d), and relative errors (e–h) of the different SZAs and distributions. Black line represents the RF calculated directly using the arithmetic mean τ. Green, blue, and red lines represent the two-point distribution, binomial distribution, and uniform distribution, respectively. (For interpretation of the references to colour in this figure legend, the reader is referred to the web version of this article.)

the two-point distribution and the uniform distribution, the relative error maximum values appears when τ is ~16 and ~22, respectively. When the maximum relative error is reached, it decreases monotonically with the increase of τ and gradually approaches 0, because the change of RF is smaller when τ becomes larger.

Correspondingly, we calculated the TOA (top of atmosphere) RF and the relative errors in different PDFs of τ (Fig. 4). The overall trend of TOA RF is similar to that of the surface, and it also shows a tendency to increase rapidly first and then stabilize. The order of relative error is: uniform distribution > two-point distribution > binomial distribution. The relative error of TOA is slightly greater than that of the surface. For example, when the SZA is 0°, the maximum relative error of the uniform distribution exceeds 16%, and the maximum relative error of the two-point distribution exceeds 12%.

4. Real cases

The nonlinear variation of RF with τ in Figs. 3 and 4 reveals that RF calculated by grid-mean τ is certainly inaccurate, and its error is affected by the distribution pattern of τ within one grid. However, the ideal experiment is simulated using an assumed perfect distribution, but the actual distribution of τ may not be perfectly described by these assumptions. Therefore, it is necessary to use actual observation data to study the error due to the gridding process. The use of MODIS cloud products provides an excellent opportunity to study this issue. Figs. 5, 6, and 7 show the original data, the average data, and the PDF of gridded τ for three different cases from MODIS observations. The dashed red line is the arithmetic mean value of the gridded τ.

Fig. 5 shows case 1 on 21 June 2016, at the junction of the mountains and plains on the southwest side of the Himalayas, where the terrain is undulating. A cloud band with a convective cell appears in the detection range of Fig. 5a, and its overall trend is consistent with the mountain trend, which is from northwest to southeast. This may be the result of the strong topographical effects and the southwesterly airflow brought by the South Asian summer monsoon (Zhang et al., 2018). The high-value region has a large τ, limited by the MODIS observing range, in which most of the values are 150, which may be the deep and intense convective cell surrounded by broad stratiform cloud and cloud anvils, introduced by Houze et al. (2007). On the northeast side of the convective cell (the plateau side), there is a large area of clear sky. The high-value center of τ is located at 28.5°N, 82°E, and is surrounded by thinner clouds with $\tau < 30$. As this high-value center occurs at the junction of two 1° × 1° grids, it is divided into two grids for calculation. After the gridding process, the high-value center shown in Fig. 5b

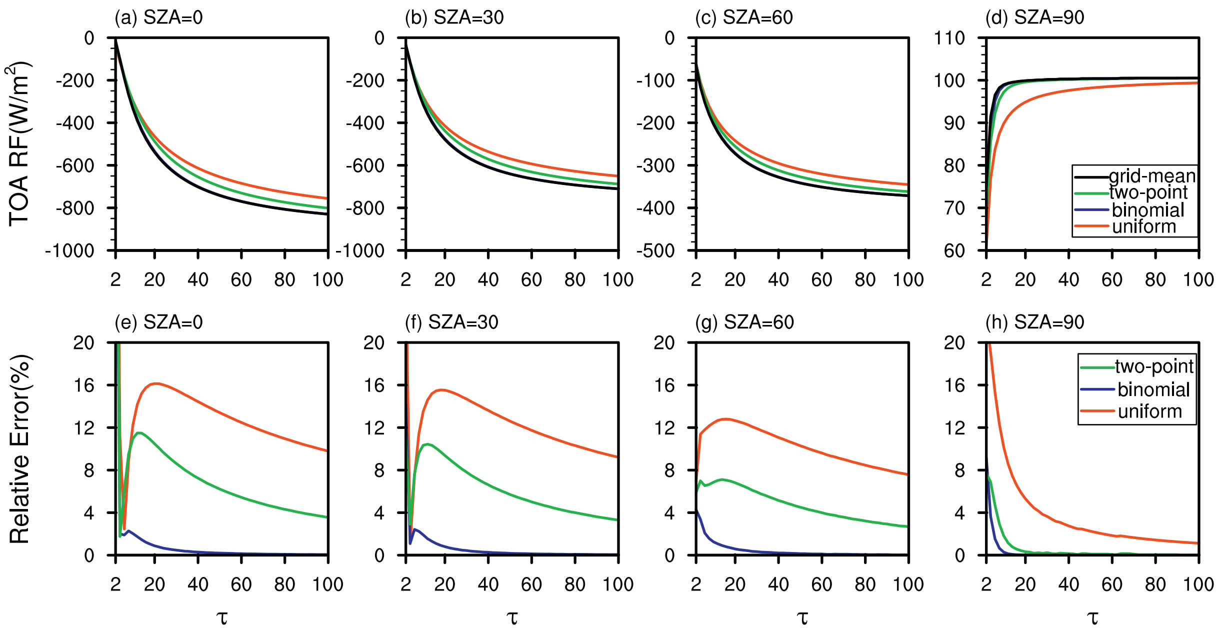

Fig. 4. TOA RF (a–d), and relative errors (e–h) of the different SZAs and distributions. Black line represents the RF calculated directly using the arithmetic mean τ. Green, blue, and red lines represent the two-point distribution, binomial distribution, and uniform distribution, respectively. (For interpretation of the references to colour in this figure legend, the reader is referred to the web version of this article.)

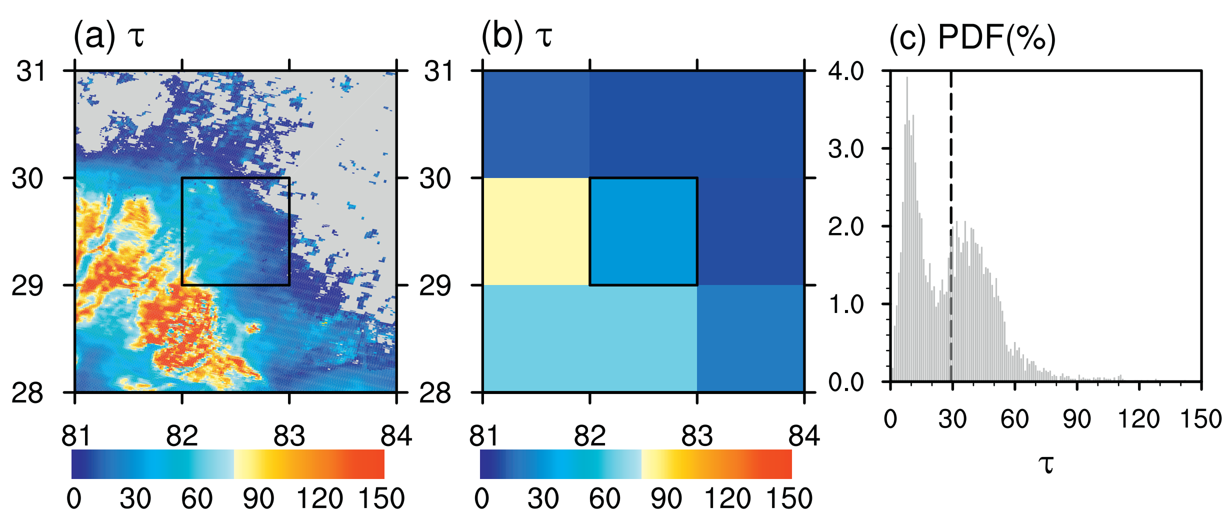

Fig. 5. Case 1, MODIS observation of τ on 21 June 2016. (a) 1 km resolution, (b) arithmetic mean in the 1° grid, and (c) PDF of the τ inside the central black box.

moves north to 29.5°N, 81.5°E (i.e. the second grid in the left column), which indicates that the cloud parameters are severely distorted by this process when describing the weather system.

The area we focus on is located on the northeast side of this convective cell, which is indicated by the black box marked in Fig. 5a. The whole grid is located at the junction of cloudy and clear skies. A small area of clear sky appears in the northeast corner of the grid. According to the MODIS algorithm, these clear-sky regions with a default value of τ were not included in the τ gridding process. The clear-sky region is surrounded by a thin cloud with an optical thickness of around 10, while the southwest corner has a small part of the optically high-value region, with values mainly distributed from 30 to 60, and up to 110. As can be seen from Fig. 5c, the PDF of τ here shows a bimodal structure. The first peak appears at around 10 and the maximum frequency is nearly 4%. The second peak is slightly wider but the peak is lower and the frequency is about 2%, distributed between 30 and 45. The arithmetic mean of the gridded τ is approximately 29 (dashed line in Fig. 5c) between the two peaks.

The example shown in Fig. 6 is from Eastern China on 2 June 2016. Fig. 6a shows that the entire 3° × 3° region is covered by cloud with τ of at least 10, with thick cloud surrounding the center grid, with a τ of up to 150. τ is very unevenly distributed in pixel-level products, but after the arithmetic averaging process (Fig. 6b), these detailed features are hard to see. The average of τ is from 30 to 50, which is very uniform. Our focus area 30–31°N, 113–114°E (black box in Fig. 6a) is located in the middle of the two high-value areas, with almost no high optical thickness values and τ of about 40. The PDF is shown in Fig. 6c, and exhibits a unimodal distribution, which approximates the binomial distribution described in the ideal experiment. The maximum value appears at τ of 35, and the peak PDF value is about 6.5%. The arithmetic mean of τ is 39.35, which is very close to the peak of the distribution.

The case shown in Fig. 7 on 16 June 2016 also occurred on the southern slope of the Himalayas. Fig. 7a shows that there is a thick cloud belt with a northwest–southeast trend in this area, and τ at the center may have exceeded the MODIS retrieval range of 150. Overall,

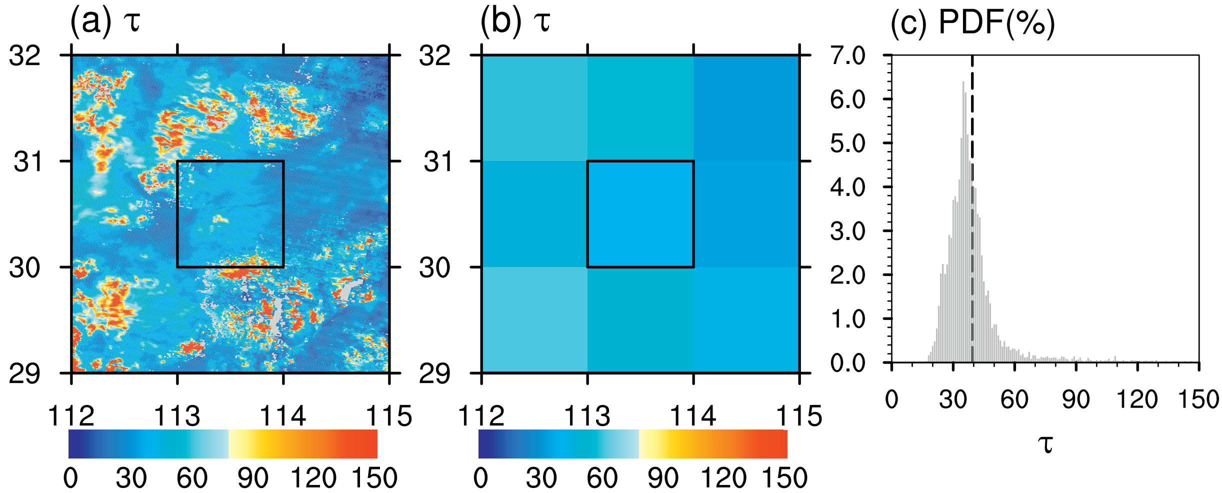

Fig. 6. Case 2, MODIS observation of τ on 2 June 2016. (a) 1 km resolution, (b) arithmetic mean in the 1° grid, and (c) PDF of the τ inside the central black box.

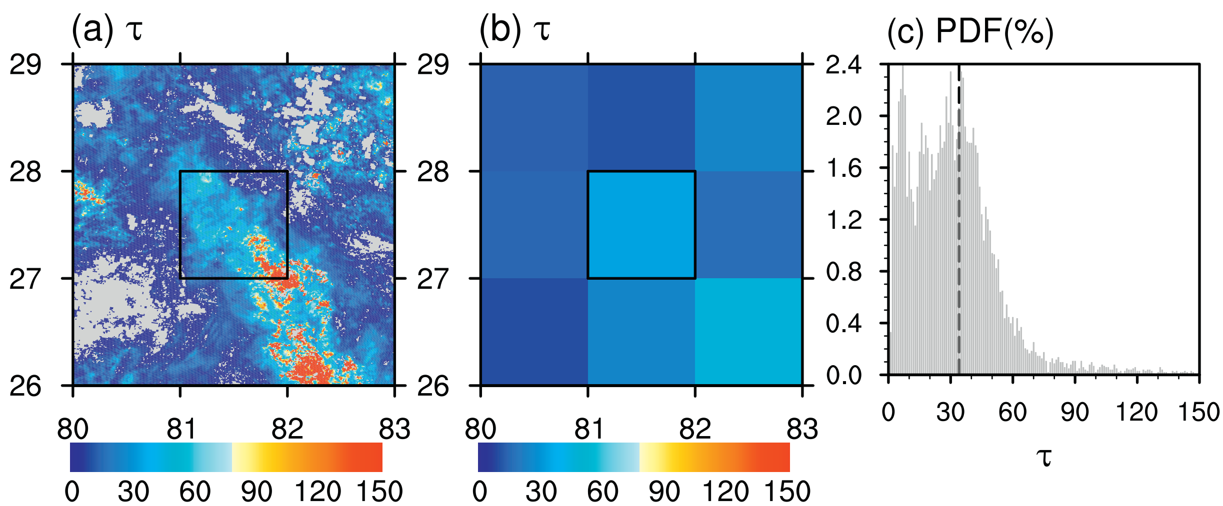

Fig. 7. Case 3, MODIS observation of τ on 16 June 2016. (a) 1 km resolution, (b) arithmetic mean in the 1° grid, and (c) PDF of the τ inside the central black box.

the thickest part of the cloud belt is mainly concentrated in the southeast, and most of the area around the cloud belt is covered by clouds with τ below 20, and in the entire 3° × 3° grid. There is little clear sky, which is mainly concentrated in the 26–27°N, 80–81°E area on the west side of the cloud band. Fig. 7b shows the τ distribution after the gridding process. The northwest–southeast trend of τ can be roughly seen, but the smoothed τ has dropped from 150 to 50. The grid we selected is in the center of the band cloud, where the overall τ is thick. At the same time, the τ distribution in this grid is shown in Fig. 7c, and the τ from 0 to 50 is maintained at around 2%, which is approximately evenly distributed in this interval. As τ further increases, its frequency rapidly decreases to zero.

Although the arithmetic mean of τ is widely used for the estimation of RF, considering its own significance, some more precise studies usually use the logarithmic mean; for example, Clouds and the Earth's Radiant Energy System (CERES) calculates the logarithmic average of τ within grids (Doelling et al., 2013; Loeb et al., 2018), for related studies of cloud RF. Fig. 8 shows the logarithmic PDF of τ of the above three cases. Fig. 8a still shows a bimodal distribution, but due to the logarithmic operation, the frequency of the right peak is significantly higher than the peak τ of 30–60 in Fig. 5c. Fig. 8b also shows a similar single-peak distribution to Fig. 6c, and its log-mean value is roughly coincident with the peak. Fig. 8c and Fig. 7c show a large difference. After the logarithmic calculation, τ from 0 to 50 becomes a unimodal distribution with a logarithmic peak of about 1.5. It is worth noting that whether it is a logarithmic PDF or an original PDF distribution, the distribution of τ within the grid points exhibits unique characteristics, rather than satisfying a normal distribution or a lognormal distribution. If τ is assumed to be a normal distribution regardless of its actual distribution pattern, a calculated deviation will inevitably occur.

Based on the arithmetic mean, the logarithmic mean and the actual pixel-level τ, we calculated their RFs respectively. For the arithmetic mean τ and the logarithmic mean τ, it is simple for RF calculation because we only need to bring the τ value into the model once. Pixel-level τ is obviously more accurate in describing τ in grid, but more complicated for RF calculation: τ of each cloudy pixel is brought into model to get the pixel-level RF, and then the pixel-level RFs in 1° grid are averaged to get the accurate RF value. Assuming the RF calculated by the pixel-level τ is the true value, the relative error of the RF simulated by the arithmetic mean τ and logarithmic mean τ is shown in Table 1. For the arithmetic mean, the relative error is greater than the RF simulated by the logarithmic mean. The distribution pattern has a great influence on the relative error. For example, the relative errors of case 1 and case 3 both exceed 15%, and since case 2 is approximately evenly distributed, the relative error is < 3%. Although the RF simulated by logarithmic mean τ is closer to the true value, it still produces a relative error of about 4% in the non-binomial cases, which is much higher than the relative error of case 2 (TOA ~0.63%, surface ~0.5%).

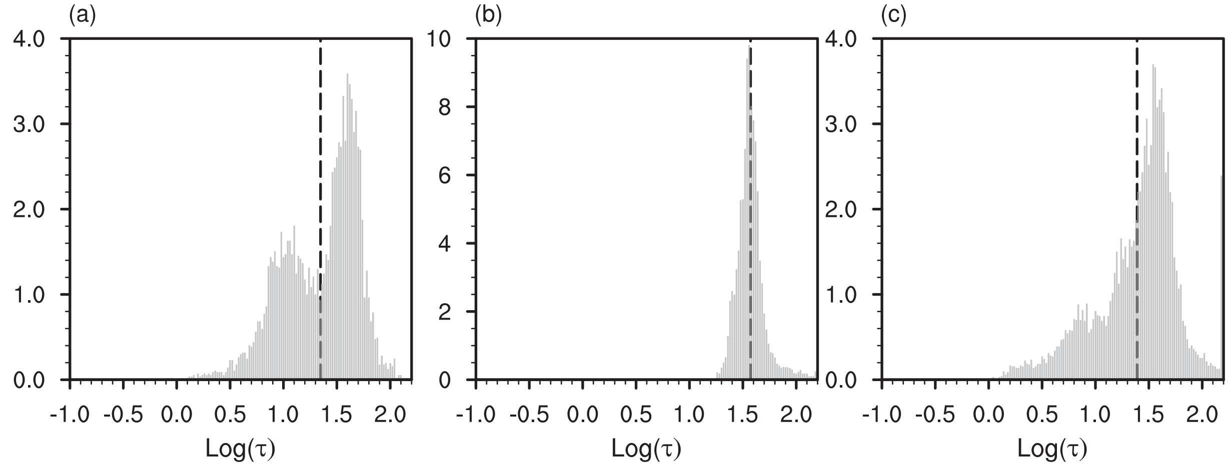

Fig. 8. Logarithmic PDF distribution of τ for the three cases: (a) case 1, (b) case 2 and (c) case 3.

Table 1
Arithmetic and logarithmic mean τ and relative error for the three cases.

Case	$\bar{\tau}$	$\bar{\tau}_{log}$	Relative error of RF(%)			
			TOA		Surface	
			Mean	Log-mean	Mean	Log-mean
1	29.23	22.39	16.7	4.1	14.2	3.3
2	39.35	37.15	2.4	0.63	2.1	0.5
3	34.07	24.55	17.2	4.2	15.2	3.5

The temporal average is also a non-negligible component in the gridding process. MODIS provides eight-day average (MOD08_E3) and monthly average (MOD08_M3) products. For a 1° grid point, the daily average product is usually only processed from 1 to 2 images of the day, while the eight-day average and monthly average products contain multiple days of observation, and the cloud parameters are more variable. Fig. 9 shows the PDFs of the τ and logarithmic τ in a 1° × 1° grid from 17 to 24 June 2016, 29–30°N, 81–82°E. Table 2 shows the relative error of the RF corresponding to the arithmetic and logarithmic mean. RF calculated by grid-mean τ is also considered inaccurate, and the RF from pixel-level τ is seen as the true value. The method of calculating relative error can be found at Section 2. The distribution of τ in Fig. 9 also could not be described by a lognormal or normal distribution, and the mean τ also has a certain deviation from the main peak of the distribution. When the radiation transfer is calculated, the error caused by the arithmetic mean is > 30%, and such high uncertainty inevitably reduces the reliability of the calculated RF. Meanwhile, the logarithmic average is also affected by the distribution pattern, and the relative errors of the surface and TOA are both > 2%.

Table 2
Relative errors of RF caused by time–space average at TOA and surface.

	TOA (%)	Surface (%)
Arithmetic	38.13	32.07
Logarithmic	2.8	2.3

5. Conclusion

In this study, SBDART is used to simulate the influence of different PDFs of τ on RF, when the mean τ in the grid is constant. The ideal experiments assume that the τ fits the two-point distribution, the binomial distribution, and the uniform distribution, respectively. For the real case studies, we used MODIS pixel-level cloud products to study the effects of space–time average on different distributions of τ, and then on the relative error of RF. The conclusions are as follows:

1. The distribution pattern of the τ within the grid has an important influence on RF. Even if the average τ of the grids is the same, the

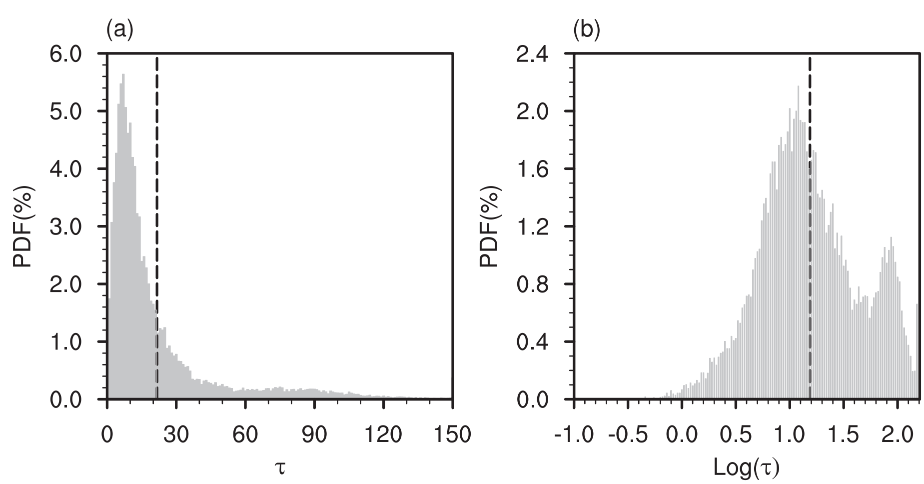

Fig. 9. (a) PDF distribution and (b) logarithmic PDF distribution of τ in the grid at 81–82°N, 29–30°N, 17–24 June 2016. The black dashed line is the arithmetic mean and logarithmic mean of τ.

unevenness of the internal τ causes a difference in RF. When τ in the grid fits the two-point distribution or uniform distribution, the relative error of the RF calculated by the arithmetic mean can reach 10–20%; for the binomial distribution, the error is small, < 5%. This shows that direct use of grid-mean τ will result in a large uncertainty in the calculation of RF, and it is necessary to focus on the distribution pattern within the grid.

2. The real case studies show that the distribution of τ within the grid is highly variable and has its own characteristics. After the gridding process, the pixel-level detailed features are smoothed. The RF calculated using the logarithmic mean τ within the grid is closer to the true value than the arithmetic mean, but there are still errors that cannot be ignored. Therefore, we hope that future grid products can fully consider the distribution pattern of pixels within the grid and establish some more representative statistics.
3. The eight-day average τ within the grid also did not show a normal distribution or a lognormal distribution. The introduction of time averaging makes the τ distribution more complicated. The relative error of RF using the arithmetic mean simulation exceeds 30%, and that using the logarithmic average is > 2%. Such large RF uncertainty caused by the distribution pattern needs sufficient attention.

There are also some limitations to this study. To avoid other errors, we controlled other parameters such as R_e, and temperature and humidity profiles as default, but these parameters also have regional differences in the grids, and they may also obey different distribution patterns, which will affect the calculation of RF. Future research may be able to couple these variables together to obtain a two-dimensional PDF or even a higher-dimensional distribution.

Acknowledgments

This work is supported by the National Natural Science Foundation of China (Grant 41675041), National Key Research and Development Program of China (Grant No. 2017YFC1501402) and the Fundamental Research Funds for the Central Universities (Grant WK6030000068).

References

Baker, M.B., 1997. Cloud microphysics and climate. Science 276, 1072–1078.
Cahalan, R.F., Ridgway, W., Wiscombe, W.J., Bell, T.L., Snider, J.B., 1994. The albedo of fractal stratocumulus clouds. J. Atmos. Sci. 51, 2434–2455.
Chen, Y., Fu, Y., 2017. Characteristics of VIRS signals within pixels of TRMM PR for warm rain in the tropics and subtropics. J. Appl. Meteorol. Clim. 56, 789–801.
Chen, Y., Fu, Y., 2018. Tropical echo-top height for precipitating clouds observed by multiple active instruments aboard satellites. Atmos. Res. 199, 54–61.
Chen, T., Rossow, W.B., Zhang, Y.C., 2000. Radiative effects of cloud-type variations. J. Clim. 13, 264–286.
Chen, Y., Fu, Y., Xian, T., Pan, X., 2017. Characteristics of cloud cluster over the steep southern slopes of the Himalayas observed by CloudSat. Int. J. Climatol. 37, 4043–4052.
Curry, J.A., Ebert, E.E., 1992. Annual cycle of radiation fluxes over the arctic-ocean-sensitivity to cloud optical-properties. J. Clim. 5, 1267–1280.
de la Torre Juarez, M., Davis, A.B., Fetzer, E.J., 2011. Scale-by-scale analysis of probability distributions for global MODIS-AQUA cloud properties: how the large scale signature of turbulence may impact statistical analyses of clouds. Atmos. Chem. Phys. 11, 2893–2901.
Doelling, D.R., Loeb, N.G., Keyes, D.F., Nordeen, M.L., Morstad, D., Nguyen, C., Wielicki, B.A., Young, D.F., Sun, M., 2013. Geostationary enhanced temporal interpolation for CERES flux products. J. Atmos Ocean Tech. 30, 1072–1090.
Fu, Y., 2014. Cloud parameters retrieved by the bispectral reflectance algorithm and associated applications. J. Meteorol. Res. 28, 965–982.
Fu, Y.F., Chen, Y.L., Li, R., Qin, F., Xian, T., Yu, L., Zhang, A.Q., Liu, G.S., Zhang, X.D., 2017. Lateral Boundary of Cirrus Cloud from CALIPSO Observations. Sci. Rep. 7, 14221.
Hannart, A., Dufresne, J.L., Naveau, P., 2009. Why climate sensitivity may not be so unpredictable. Geophys. Res. Lett. 36.
Houze, R.A., Wilton, D.C., Smull, B.F., 2007. Monsoon convection in the Himalayan region as seen by the TRMM Precipitation Radar. Q. J. R. Meteor. Soc. 133, 1389–1411.
Kienast-Sjogren, E., Rolf, C., Seifert, P., Krieger, U.K., Luo, B.P., Kramer, M., Peter, T., 2016. Climatological and radiative properties of midlatitude cirrus clouds derived by automatic evaluation of lidar measurements. Atmos. Chem. Phys. 16, 7605–7621.
King, M.D., Tsay, S.C., Platnick, S.E., Wang, M., Liou, K.N., 1997. Cloud Retrieval Algorithms for MODIS: Optical Thickness, Effective Particle Radius, and Thermodynamic Phase.
Li, R., Cai, H.K., Fu, Y.F., Wang, Y., Min, Q.L., Guo, J.C., Dong, X., 2014. The optical properties and longwave radiative forcing in the lateral boundary of cirrus cloud. Geophys. Res. Lett. 41, 3666–3675.
Liou, K.N., 2002. An Introduction to Atmospheric Radiation. Academic Press.
Liu, H., Yeh, R., Cai, B., 2017. Reliability modeling for dependent competing failure processes of damage self-healing systems. Comput. Ind. Eng. 105, 55–62.
Loeb, N.G., Doelling, D.R., Wang, H., Su, W., Nguyen, C., Corbett, J.G., Liang, L., Mitrescu, C., Rose, F.G., Kato, S., 2018. Clouds and the earth's radiant energy system (CERES) energy balanced and filled (ebaf) top-of-atmosphere (TOA) edition-4.0 data product. J. Clim. 31, 895–918.
Nakajima, T., King, M.D., 1990. Determination of the optical thickness and effective particle radius of clouds from reflected solar radiation measurements. Part I: Theory. J. Atmos. Sci. 47, 1878–1893.
Nakajima, T.Y., Nakajima, T., 1995. Wide-area determination of cloud microphysical properties from NOAA AVHRR measurements for FIRE and ASTEX regions. J. Atmos. Sci. 52, 4043–4059.
Oreopoulos, L., Davies, R., 1998. Plane parallel albedo biases from satellite observations. Part I: dependence on resolution and other factors. J. Clim. 11, 919–932.
Oreopoulos, L., Platnick, S., Hong, G., Yang, P., Cahalan, R.F., 2009. The shortwave radiative forcing bias of liquid and ice clouds from MODIS observations. Atmos. Chem. Phys. 9, 5865–5875.
Pierrehumbert, R.T., 1996. Anomalous scaling of high cloud variability in the tropical Pacific. Geophys. Res. Lett. 23, 1095–1098.
Platnick, S., Meyer, K.G., King, M.D., Wind, G., Amarasinghe, N., Marchant, B., Arnold, G.T., Zhang, Z., Hubanks, P.A., Holz, R.E., Yang, P., Ridgway, W.L., Riedi, J., 2017. The MODIS cloud optical and microphysical products: collection 6 updates and examples from Terra and Aqua. Ieee T Geosci. Remote 55, 502–525.
Ramanthan, V., 1989. Cloud-radiative forcing and climate: results from the earth radiation budget experiment. Science 243, 57–63.
Rangno, A.L., Hobbs, P.V., 2005. Microstructures and precipitation development in cumulus and small cumulonimbus clouds over the warm pool of the tropical Pacific Ocean. Q. J. R. Meteor. Soc. 131, 639–673.
Ricchiazzi, P., Yang, S.R., Gautier, C., Sowle, D., 1998. SBDART: a research and teaching software tool for plane-parallell radiative transfer in the Earth's atmosphere. B. Am. Meteorol. Soc. 79, 2101–2114.
Riley, E.M., Mapes, B.E., 2009. Unexpected peak near-15 degrees C in CloudSat echo top climatology. Geophys. Res. Lett. 36.
Roe, G.H., Baker, M.B., 2007. Why is climate sensitivity so unpredictable? Science 318, 629–632.
Rosenfeld, D., Dai, J., Yu, X., Yao, Z., Xu, X., Yang, X., Du, C., 2007. Inverse relations between amounts of air pollution and orographic precipitation. Science 315, 1396–1398.
Rossow, W.B., Schiffer, R.A., 1999. Advances in understanding clouds from ISCCP. B. Am. Meteorol. Soc. 80, 2261–2287.
Stamnes, K., Tsay, S.C., Wiscombe, W., Jayaweera, K., 1988. Numerically stable algorithm for discrete-ordinate-method radiative-transfer in multiple-scattering and emitting layered media. Appl. Opt. 27, 2502–2509.
Yang, Y., Fu, Y., Qin, F., Zhu, J., 2017. Radiative forcing of the tropical thick anvil evaluated by combining TRMM with atmospheric radiative transfer model. Atmos. Sci. Lett. 18, 222–229.
Zhang, A., Fu, Y., Chen, Y., Liu, G., Zhang, X., 2018. Impact of the surface wind flow on precipitation characteristics over the southern Himalayas: GPM observations. Atmos. Res. 202, 10–22.